


**Band-engineered bilayer Haldane model: Evidence of multiple topological phase transitions**Sayan Mondal  and Saurabh Basu*Department of Physics, Indian Institute of Technology Guwahati, Guwahati 781039, Assam, India* (Received 9 April 2023; revised 10 June 2023; accepted 11 July 2023; published 25 July 2023)

We have studied the evolution of the topological properties of a band-engineered, AB-stacked bilayer honeycomb structure in the presence of a Haldane flux. Without a Haldane flux, band engineering makes the band touching points (the so-called Dirac points) move towards each other and eventually merge into one at an intermediate  $\mathbf{M}$  point in the Brillouin zone. Here the dispersion is linear along one direction and quadratic along the other. In the presence of a Haldane flux, the system acquires topological properties, and finite Chern numbers can be associated with the pairs of the conduction and the valence bands. The valence band closer to the Fermi level ( $E_F$ ) possesses Chern numbers equal to  $\pm 2$  and  $\pm 1$ , while the one further away from  $E_F$  corresponds to Chern numbers  $\pm 1$ . The conduction bands are associated with similar properties, except their signs are reversed. The Chern lobes shrink in the band-engineered model, and we find evidence of multiple topological phase transitions, where the Chern numbers discontinuously jump from  $\pm 2$  to  $\mp 2$ ,  $\pm 1$  to  $\mp 1$ ,  $\pm 1$  to 0 to  $\pm 2$ , and  $\pm 2$  to  $\pm 1$ . These transitions are supported by the presence or absence of the chiral edge modes in a nanoribbon bilayer geometry and the vanishing of the plateau in the anomalous Hall conductivity. Different phases are further computed for different hopping amplitudes across the layers, which shows shrinking of the Chern lobes for large interlayer tunneling.

DOI: [10.1103/PhysRevB.108.045307](https://doi.org/10.1103/PhysRevB.108.045307)**I. INTRODUCTION**

The Haldane model is a toy model, where it was shown that one can achieve quantum Hall effect even in the absence of an external magnetic field in a two-dimensional honeycomb lattice [1]. To achieve such a scenario, the time-reversal symmetry (TRS) of the system needs to be broken, which can be done via chiral, complex next-nearest-neighbor hopping amplitudes. The spectral bands of such a system possess a nonzero topological invariant known as the Chern number.

The Haldane model is a single-layer system; however, layered Dirac systems are interesting to study owing to the quadratic band dispersion, along with a spectral gap (proportional to the interlayer tunneling amplitude) at the Dirac points. These features are in contrast with its monolayer counterpart. In recent years there have been studies of the Haldane model in coupled two-dimensional systems, for example, the bilayer materials [2–5], Moiré lattices [6–10], etc. In parallel, there are studies on the band engineering in various systems, such as, single-layer graphene [11], spin Hall insulators [12], and a dice lattice [13]. Such a band engineering has been incorporated via the introduction of an anisotropy among the nearest-neighbor (NN) hoppings. Such hopping anisotropies have been included between the neighboring sites lying along a particular direction (say,  $t_1$ ), while keeping the rest NN hoppings as  $t$  in a honeycomb lattice. If the value of  $t_1$  is varied, the band extrema from the two Dirac points move closer to each other, and they finally merge with a vanishing band gap at the  $\mathbf{M}$  point in the Brillouin zone (BZ) for a particular value of  $t_1$ , namely,  $t_1 = 2t$ , which is called the semi-Dirac limit. During the process, the topological properties of the system also vanish at the gap-closing hopping amplitude  $t_1 = 2t$ . It should be noted that the band structure of the system in absence of the complex next-NN (NNN) hopping (Haldane flux) shows

semi-Dirac dispersion, that is, linear along the  $k_x$  direction and quadratic along the  $k_y$  direction. Experimentally, the semi-Dirac dispersion has been observed in many materials, such as multilayered structures of  $\text{TiO}_2/\text{VO}_2$  [14,15], monolayer phosphorene in the presence of doping and pressure [16,17], BEDT – TTF<sub>2</sub>I<sub>3</sub> organic salts under pressure [18,19], black phosphorus doped with potassium atoms by means of *in situ* deposition [20], etc. One can also achieve the semi-Dirac dispersion by applying a uniaxial strain to a system which will change the bond length lying along a particular direction that is parallel to the applied strain direction. Therefore, the hopping energies along those directions are modified, while the hopping along the other directions remains unaltered. Such a method has been employed in a monolayer honeycomb structure, such as  $\text{Si}_2\text{O}$ , which yields a semi-Dirac dispersion [21].

However, the effect of band engineering in a multilayered system, such as a bilayer graphene, has never been studied. Needless to mention, bilayers possess a richer phase diagram comprised of a larger parameter space. The topological properties of such an engineered system are interesting, since the existence of the edge modes and the quantized Hall conductivity have never been studied. A more interesting issue is that owing to larger numbers of bands being present in the band structure of a bilayer system, higher values of Chern numbers are realized. A higher Chern number implies higher value of the anomalous Hall conductivity, together with a larger number of chiral edge modes present in a semi-infinite system.

Higher Chern numbers are in general interesting and can be realized in a host of systems, such as in the Dirac [22] and semi-Dirac [23] systems in the presence of longer range hopping, multiorbital triangular lattices [24], star lattices or decorated honeycomb lattices [25], honeycomb lattices in the

presence of spin-orbit coupling [26,27], ultracold gases in triangular lattices [28,29], etc. Further, topological insulators doped with magnetic materials [30], Cr-doped thin laminar sheets of  $\text{Bi}_2(\text{Se}, \text{Te})_3$  [31], also demonstrate higher values of the Chern numbers. Further,  $\text{MnBi}_2\text{Te}_4$  at high temperature [32,33], multilayered structures of doped (with magnetic materials) and undoped topological insulators arranged alternatively [34], and classical systems such as sonic crystals prepared using acoustic components [35] show nontrivial phases with higher Chern numbers.

In this work we focus on a bilayer graphene with broken TRS, that is, a coupled bilayer Haldane model. The stacking of the two layers is assumed in such a way that the B sublattice of the upper layer lies exactly above the A sublattice of the lower layer. Such stacking is known as AB stacking or the Bernal stacking. We shall see that the Chern numbers associated with various bands reveal interesting properties. For example, some of the bands possess both Chern numbers  $\pm 2$  and  $\pm 1$ , while the rests are associated with Chern numbers  $\pm 1$ . Such a scenario needs to be assessed for a band-engineered system. Specifically, we wish to address the ramifications of the band deformation caused via asymmetric hopping amplitudes on the topological properties and ascertain whether such deformation induces a topological phase transition. In our bilayer model, the band engineering is incorporated via asymmetric NN hopping amplitudes in each of the layers, while the tunneling amplitude across the layers is left unaltered.

Our subsequent discussions have been arranged as follows. Section II introduces the tight-binding Hamiltonian of a bilayer graphene. Section III discusses the band structure of the system with the interlayer coupling ( $t_\perp$ ) and the anisotropic NN hopping amplitudes ( $t_1$ ) as parameters. Section IV deals with the phase diagrams that are obtained by computing the Chern numbers associated with the bands. In Sec. V the presence (or absence) of the chiral edge modes in a ribbon geometry are presented. Next, the numerical computations of the anomalous Hall conductivity are shown in Sec. VI. Finally, a brief summary of the results are included in the concluding section (Sec. VII).

## II. THE HAMILTONIAN

A tight-binding Hamiltonian of a bilayer honeycomb lattice can be written as follows:

$$H = \sum_{p \in l, u} \left[ \sum_{\langle ij \rangle} t_{ij} c_i^{p\dagger} c_j^p + t_2 \sum_{\langle\langle im \rangle\rangle} e^{i\phi_p^{im}} c_i^{p\dagger} c_m^p + \text{H.c.} \right] + \left[ t_\perp \sum_{\langle q, r \rangle_\perp} c_q^{l\dagger} c_r^u + \text{H.c.} \right], \quad (1)$$

where  $c_i^{p\dagger}$  ( $c_i^p$ ) is the creation (annihilation) operator corresponding to site  $i$ , which belongs to the layer  $p$ . Here  $p = l, u$  represent the lower and the upper layers, respectively. The first term on the right-hand side denotes the NN hopping with the amplitude  $t_{ij}$  being either  $t_1$  when  $i$  and  $j$  sites lie along the  $\delta_1 = a_0(0, 1)$  direction, or  $t$  when they lie along the  $\delta_2 = a_0(\sqrt{3}/2, -1/2)$  and  $\delta_3 = a_0(\sqrt{3}/2, -1/2)$  directions,

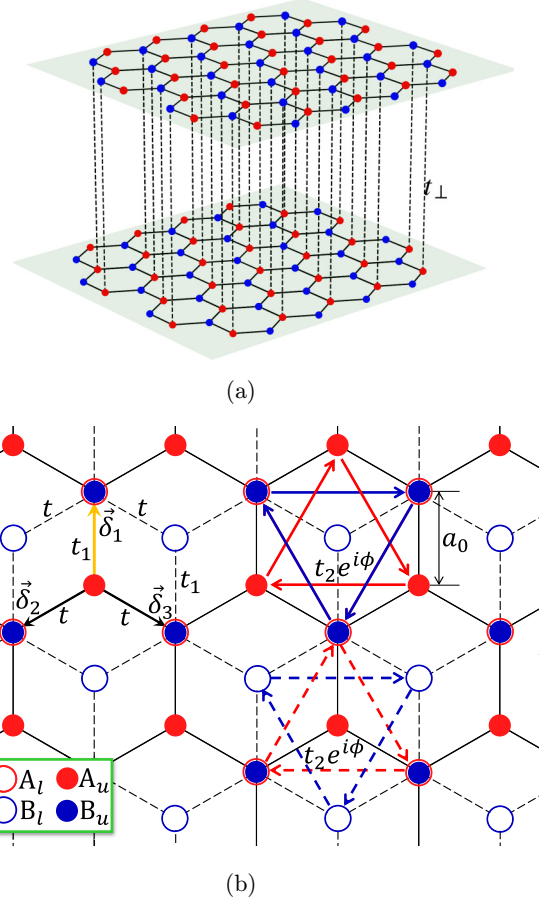


FIG. 1. A bilayer graphene is shown in (a) with the interlayer coupling  $t_\perp$  between the B sublattice of the upper layer and the A sublattice of the lower layer. In both layers, the A and B sublattices are denoted by the red and blue filled circles. In (b), the other planar hoppings are shown. To properly see each sublattice in each layer, we have denoted the A and B sublattices in the lower layer with the circles in red and blue, respectively. The subscripts  $l$  and  $u$  in  $A_{l,u}$  and  $B_{l,u}$  refer to the lower and upper layer, respectively. All the bondings and NNN hoppings in the lower layers are shown by the dashed lines and dashed arrows, respectively. The NN hopping strength along the  $\delta_1$  direction (shown via the yellow arrow) is  $t_1$ , while it is  $t$  along the  $\delta_{2,3}$  directions ( $\delta_i$  are defined in text). The NNN hopping is  $t_2 e^{i\phi}$  ( $t_2 e^{-i\phi}$ ) for the clockwise (counterclockwise) direction.

as shown in Fig. 1. The second term represents the complex NNN hopping with the amplitude  $t_2$  and a phase  $\phi_{l,p}^{im}$ . We have labeled the Haldane flux corresponding to the lower and upper layers as  $\phi_l^{im}$  and  $\phi_u^{im}$ , respectively. If an electron hops in the counterclockwise direction,  $\phi_{l,p}^{im}$  assumes a positive sign, while for the clockwise direction it acquires negative sign. The third term is the hopping between the two layers with the coupling strength  $t_\perp$ . It should be kept in mind that the interlayer hopping is between the B sublattice on layer  $u$  ( $r \in B_u$ ) and the A sublattice on layer  $l$  ( $q \in A_l$ ) (AB or Bernal stacking). In our calculations we have varied  $t_1$  in both the layers from a value  $t$  to  $2t$  (semi-Dirac) and even considered  $t_1 > 2t$ .

Now we Fourier transform the Hamiltonian and write them in the four sublattice basis, namely,  $\{A_l, B_l, A_u, B_u\}$ , in the

following way:

$$H(\mathbf{k}) = \begin{pmatrix} h_z^+(\mathbf{k}, \phi_l) & h_{xy}(\mathbf{k}, t_1) & 0 & t_\perp \\ h_{xy}^*(\mathbf{k}, t_1) & h_z^-(\mathbf{k}, \phi_l) & 0 & 0 \\ 0 & 0 & h_z^+(\mathbf{k}, \phi_u) & h_{xy}(\mathbf{k}, t_1) \\ t_\perp & 0 & h_{xy}^*(\mathbf{k}, t_1) & h_z^-(\mathbf{k}, \phi_u) \end{pmatrix}, \quad (2)$$

where  $h_z^\pm$  are defined as  $h_z^\pm(\mathbf{k}, \phi_p) = h_0(\mathbf{k}, \phi_p) \pm h_z(\mathbf{k}, \phi_p)$ . The element  $h_{xy}(\mathbf{k}, t_1)$  has the following form:  $h_{xy}(\mathbf{k}, t_1) = h_x(\mathbf{k}, t_1) - ih_y(\mathbf{k}, t_1)$ . The expressions for the  $h_i$ s can be written as

$$h_0(\mathbf{k}, \phi_p) = 2t_2 \cos \phi_p \left\{ 2 \cos \frac{\sqrt{3}k_x}{2} \cos \frac{3k_y}{2} + \cos \sqrt{3}k_x \right\}, \quad (3)$$

$$h_z(\mathbf{k}, \phi_p) = -2t_2 \sin \phi_p \left\{ 2 \sin \frac{\sqrt{3}k_x}{2} \cos \frac{3k_y}{2} - \sin \sqrt{3}k_x \right\}, \quad (4)$$

$$h_x(\mathbf{k}, t_1) = \left\{ t_1 \cos k_y + 2t \cos \frac{k_y}{2} \cos \frac{\sqrt{3}k_x}{2} \right\}, \quad (5)$$

and

$$h_y(\mathbf{k}, t_1) = \left\{ -t_1 \sin k_y + 2t \sin \frac{k_y}{2} \cos \frac{\sqrt{3}k_x}{2} \right\}. \quad (6)$$

Throughout our work, the amplitude of the NNN hopping  $t_2$  is kept fixed at  $0.1t$ , and two different values of the interlayer hopping strength are chosen, namely,  $t_\perp = 0.5t$  and  $t_\perp = 0.1t$  [36]. The values of  $\phi_l$  and  $\phi_u$  are taken such that  $\phi_l = \phi_u = \pi/2$ . Now, for  $\phi_u = \phi_l$ , we obtain the following dispersion relation:

$$E_\pm^c = \left[ h_0 + \sqrt{\frac{t_\perp^2}{2} + |h_{xy}|^2 + h_z^2} \pm \frac{t_\perp}{2} \sqrt{t_\perp^2 + 4h_{xy}^2} \right], \quad (7)$$

$$E_\pm^v = \left[ h_0 - \sqrt{\frac{t_\perp^2}{2} + |h_{xy}|^2 + h_z^2} \pm \frac{t_\perp}{2} \sqrt{t_\perp^2 + 4h_{xy}^2} \right], \quad (8)$$

where  $E_\pm^c$  denote the two conduction bands and  $E_\pm^v$  are the two valence bands for a bilayer.

### III. SPECTRAL PROPERTIES

In this section we discuss how the spectral properties evolve as we interpolate between the Dirac and the semi-Dirac limits. We show the band structure for two different values of  $t_\perp$ . The first one is for  $t_\perp = 0.5t$ , as shown in Fig. 2. As can be seen, there are four bands which we have labeled as follows. The upper conduction band is labeled as band c1, while the lower conduction band is band c2. Similarly, the lower and the upper valence bands are labeled as band v1 and band v2, respectively. When  $t_2 = 0$  (no Haldane flux), band c2 and band v2 touch each other at the Fermi level

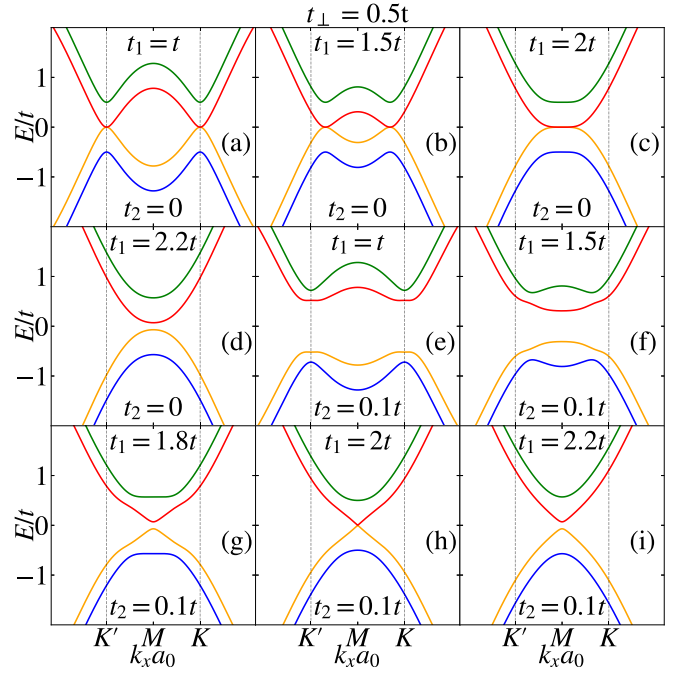


FIG. 2. The band structure in absence of  $t_2$  ( $t_2 = 0$ ) is shown along the  $k_x$  axis (at  $k_y a_0 = 2\pi/3$ ) for (a)  $t_1 = t$ , (b)  $t_1 = 1.5t$ , (c)  $t_1 = 2t$ , and (d)  $t_1 = 2.2t$ . Similarly, the dispersions in the presence of  $t_2$  ( $t_2 = 0.1t$ ) are depicted for (e)  $t_1 = t$ , (f)  $t_1 = 1.5t$ , (g)  $t_1 = 1.8t$ , (h)  $t_1 = 2t$ , and (i)  $t_1 = 2.2t$ . The values of the other parameters are  $t_\perp = 0.5t$  and  $\phi_l = \phi_u = \pi/2$ .

at the  $\mathbf{K}$  and  $\mathbf{K}'$  points [see Figs. 2(a)–2(d)]. These points are referred to as the Dirac points. Further, with the increase in the value of  $t_1$ , we deviate from the Dirac limit, and the band touching points move close to each other, which finally merge at  $t_1 = 2t$ . Beyond this value, that is, for  $t_1 > 2t$ , a gap opens up at the  $\mathbf{M}$  point. Now, if we switch on  $t_2$  [see Figs. 2(e)–2(i)], the spectral gap remains open for  $t \leq t_1 < 2t$  and  $t_1 > 2t$ , while the gap vanishes exactly at the semi-Dirac limit, namely,  $t_1 = 2t$ . The gap-closing scenario of the bilayer graphene is thus similar to the case of single-layer graphene, where the energy gap between the conduction and valence band vanishes at the semi-Dirac limit, that is, at  $t_1 = 2t$  [11].

Further, we have presented band structure in Fig. 3 for a smaller value of  $t_\perp$ , namely,  $t_\perp = 0.1t$ . It is obvious from Eqs. (7) and (8) that the separation among the conduction bands (band c1 and band c2) and that among the valence bands (band v1 and band v2) decreases with decrease in  $t_\perp$ . Moreover, the low energy dispersions of band c2 and band v2 about the band touching points have a linear behavior which was quadratic for  $t_\perp = 0.5t$ . Thus the massive electrons become progressively massless as we lower the value of  $t_\perp$ . Further, with the decrease in  $t_\perp$ , the spectral gap between band c2 and band v2 increases. For example, when  $t_\perp = 0.1t$  the band gap is  $\Delta E_g \simeq 1.0390t$  and  $0.3124t$  for  $t_1 = t$  and  $1.8t$ , respectively, while for  $t_\perp = 0.5t$ ,  $\Delta E_g \simeq 1.0335t$  and  $0.1406t$  for  $t_1 = t$  and  $1.8t$ , respectively. Thus the difference in energy is more noticeable as we move towards the semi-Dirac limit, that is, at large values of  $t_1$ .

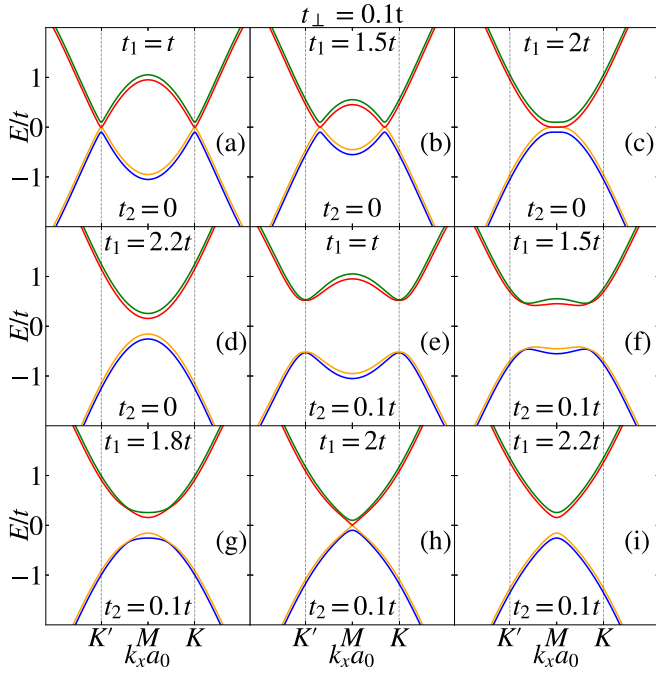


FIG. 3. The band structure for  $t_2 = 0$  is shown along the  $k_x$  axis (at  $k_y a_0 = 2\pi/3$ ) for (a)  $t_1 = t$ , (b)  $t_1 = 1.5t$ , (c)  $t_1 = 2t$ , and (d)  $t_1 = 2.2t$ . The spectra for a nonzero  $t_2$  ( $t_2 = 0.1t$ ) are depicted for (e)  $t_1 = t$ , (f)  $t_1 = 1.5t$ , (g)  $t_1 = 1.8t$ , (h)  $t_1 = 2t$ , and (i)  $t_1 = 2.2t$ . The values of  $t_\perp$ ,  $\phi_l$ , and  $\phi_u$  are fixed at  $0.1t$ ,  $\pi/2$ , and  $\pi/2$ , respectively.

#### IV. CHERN NUMBER AND PHASE DIAGRAM

In this section we calculate the Chern number as a function of the Haldane flux of the two layers. Owing to the broken TRS, the bands possess nonzero Chern numbers, which can be calculated by integrating the Berry curvature over the BZ [37,38]:

$$C = \frac{1}{2\pi} \iint_{\text{BZ}} \Omega(k_x, k_y) dk_x dk_y, \quad (9)$$

where  $\Omega(k_x, k_y)$  is the  $z$  component of the Berry curvature [39], which is obtained from the following relation:

$$\Omega(k_x, k_y) = -2i \text{Im} \left[ \left\langle \frac{\partial \psi(k_x, k_y)}{\partial k_x} \middle| \frac{\partial \psi(k_x, k_y)}{\partial k_y} \right\rangle \right], \quad (10)$$

where  $\psi(k_x, k_y)$  is the periodic part of the Bloch wave corresponding to the Hamiltonian defined in Eq. (2), and  $\text{Im}$  denotes the imaginary part. Hence we calculate the Chern numbers as a function of the fluxes  $\phi_l$  and  $\phi_u$  corresponding to band v1 for various values of  $t_1$ , as shown in Fig. 4. Here the value of  $t_\perp$  is chosen to be  $0.5t$ . We have denoted the Chern insulating regions by two colors. The regions in red denote the  $C = +1$  phase, while the blue ones denote  $C = -1$  phases. The trivial phases with  $C = 0$  are shown by the white regions. It is evident from Fig. 4(a) that the areas of the Chern insulating regions are maximum for  $t_1 = t$  (Dirac case). An engineering of the band structure, that is, with the increase in the value of  $t_1$ , the area of the topological regions (called the Chern lobes) gradually shrink. We have shown the phase diagram till a certain value, namely,  $t_1 = 1.9t$  (see Fig. 4(d)), beyond which the topological regions can hardly

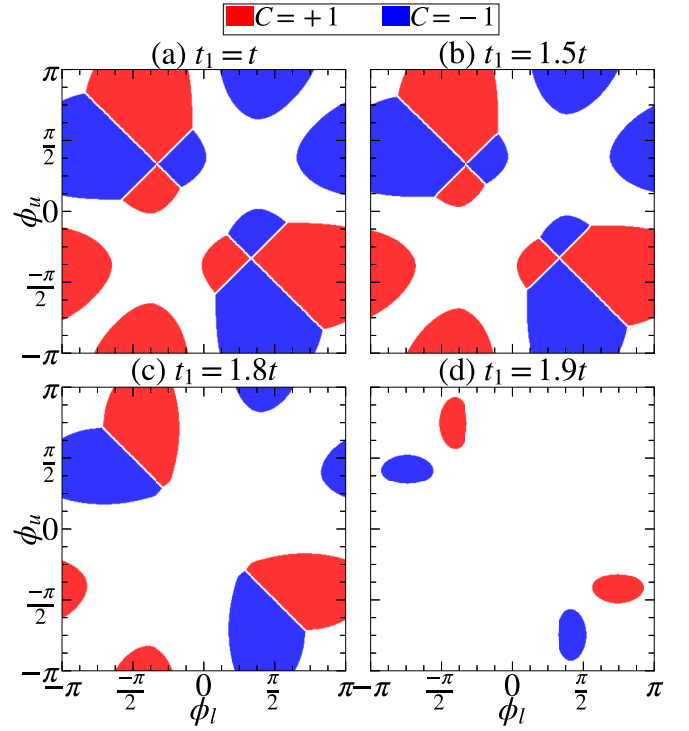


FIG. 4. The phase diagrams corresponding to the lowest occupied band, that is, band v1, is presented for  $t_\perp = 0.5t$ . The white regions denote the trivial phase with Chern number as zero, while the colored regions indicate the nontrivial phase with the nonzero Chern numbers. The nonzero values are indicated at the top of the figure.

be seen. When  $t_1$  becomes equal to  $2t$ , the Chern number ( $C$ ) vanishes completely for all values of  $\phi_l$  and  $\phi_u$  owing to a gapless scenario between band c2 and band v2. Although band v1 remains separated from band v2, the Chern number still vanishes. For  $t_1 > 2t$ , a gap opens up; however, the Chern numbers continue to be zero, and thus the gap is trivial.

Further, we have presented the phase diagrams corresponding to band v2 (the one closer to the Fermi level) in Fig. 5. As can be seen, additional phases with higher Chern number ( $C = \pm 2$ ) appear. We have denoted the  $C = +2$  and  $C = -2$  phase with cyan and green colors, respectively. The red and blue colors continue to denote  $C = +1$  and  $C = -1$  phases, respectively. Thus, both  $C = \pm 2$  and  $C = \pm 1$  phases occur at different parameter values in the same phase diagram. Further, the topological regions shrink with the increase in  $t_1$  and finally vanish at  $t_1 = 2t$ , where the gap between band v2 and c2 vanishes. For  $t_1 > 2t$ , the gap reopens, but the Chern number remains zero for all values of  $\phi_l$  and  $\phi_u$ . The phase diagrams for bands c1 and c2 are identical in shape to those of bands v1 and v2, respectively, except the Chern numbers have opposite signs.

We present the Berry curvature ( $\Omega$ ) plots corresponding to bands v1 and v2 in Fig. 6. As can be seen, the values for  $\Omega$  are highly concentrated around the band extrema points. Since with the inclusion of an anisotropic hopping ( $t < t_1 \leq 2t$ ) the two band extrema move close to each other, we observe the migration of the regions with finite and large values of  $\Omega$  towards each other in the plots [seen via the distortion of the



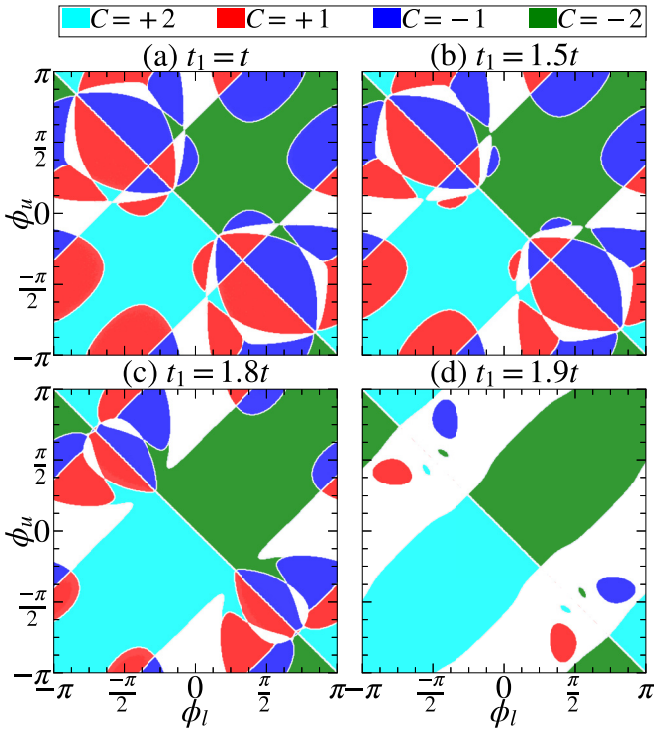


FIG. 5. The phase diagrams corresponding to band v2 are presented for  $t_{\perp} = 0.5t$ . The white regions denote the trivial phases with zero Chern number, while the colored regions indicate the nontrivial phase with the nonzero Chern numbers. Again, the values are indicated at the top of the figure.

honeycomb structure in Figs. 6(b)–6(d) and Figs. 6(f)–6(h)]. It should be noted that the Chern number for band v2 is  $-2$  for  $t_1 < 2t$ , while that corresponding to band v1 is zero at  $\pi/2$  Haldane flux, that is,  $\phi_l = \phi_u = \pi/2$ . However, we always get nonzero values for the Berry curvature for all values of  $t_1$  corresponding to both band v1 [Figs. 6(a)–6(d)] and band v2 [Figs. 6(e)–6(h)], since the time-reversal symmetry remains broken all throughout. Moreover, the Berry curvature plots show evidence of sign reversal for  $t_1 > 2t$ , namely,  $t_1 = 2.2t$ , as shown in Fig. 6(h). Thus, in certain situations, a finite Berry curvature may lead to zero Chern number.

To probe further into the gap-closing scenario associated with different phase transitions occurring in the phase diagrams, the band structures are presented in Fig. 8 for a particular value of  $t_1$  and  $t_{\perp}$ , namely,  $t_1 = t$  and  $t_{\perp} = 0.5t$ . The values of  $\phi_l$  and  $\phi_u$  are such that they lie along the four lines, namely,  $L_1$ ,  $L_2$ ,  $L_3$ , and  $L_4$  in the phase diagrams depicted in Fig. 7, and are denoted by  $\eta_i$  ( $i = 1, \dots, 6$ ),  $\gamma_j$  ( $j = 1, \dots, 9$ ), and  $\chi_s$  ( $s = 1, 2, 3$ ). Along  $L_1$ , a topological phase transition occurs between  $C = +2$  and  $C = -2$  corresponding to band v2, while the transition between  $C = +1$  and  $C = -1$  occurs along  $L_2$  for both band v2 and band v1. These results have to be understood in conjunction with the corresponding band structures as shown in Figs. 8(a)–8(c) and 8(d)–8(f), respectively. The band structures corresponding to  $\eta_1$  and  $\eta_3$  points are identical, and the Chern numbers corresponding to band v2 are  $+2$  and  $-2$ , respectively [Fig. 7(a)]. At  $\eta_2$ , bands v2 and c2 touch each other at both the Dirac points [Fig. 8(b)], and hence there is a phase transition at  $\eta_2$ . However, band v1

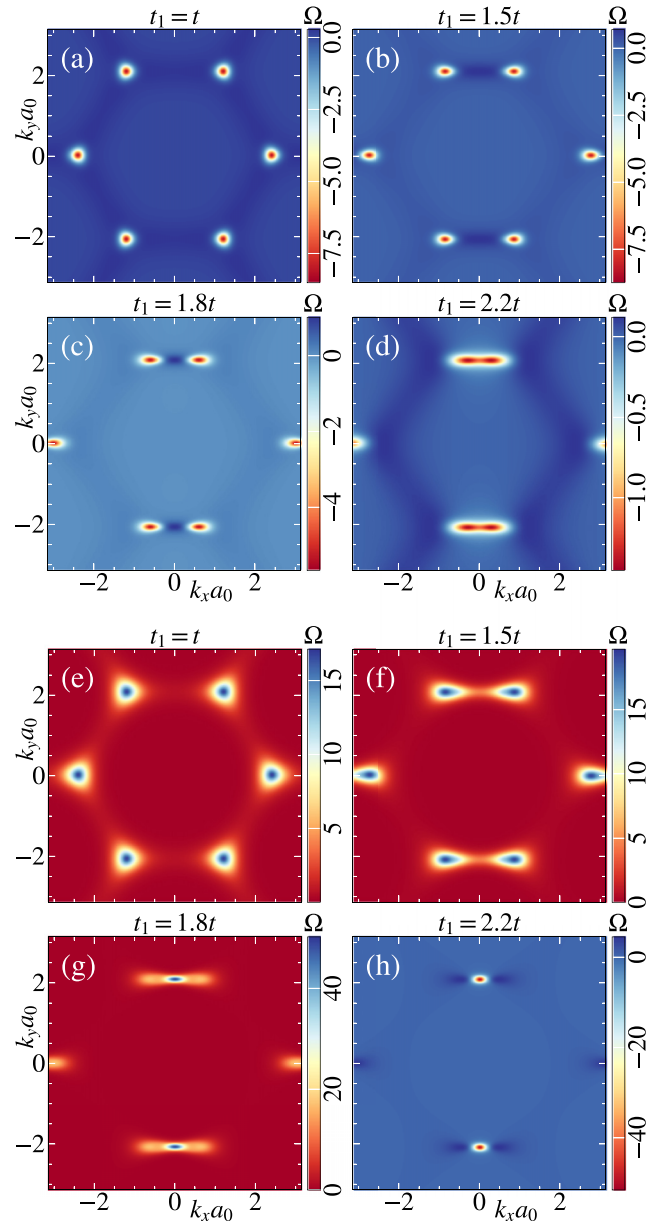


FIG. 6. The Berry curvatures are depicted for  $t_1 = t$  in (a) and (e),  $t_1 = 1.5t$  in (b) and (f),  $t_1 = 1.8t$  in (c) and (g), and  $t_1 = 2.2t$  in (d) and (h). [(a)–(d)] correspond to the Berry curvature of band v1, while [(e)–(h)] correspond to those of band v2. The values of other parameters are as follows:  $\phi_l = \phi_u = \pi/2$ ,  $t_{\perp} = 0.5t$ , and  $t_2 = 0.1t$ .

remains isolated from band v2 at these  $\eta$  points, and the Chern numbers are zero along  $L_1$ , as evident from its phase diagram [Fig. 7(c)]. Further, the band structures corresponding to  $\eta_4$  and  $\eta_6$  have similar features; however, in this case  $C$  has values of  $+1$  and  $-1$ , respectively, corresponding to band v2, while for band v1,  $C$  has the same magnitude but of opposite signs. At the phase transition occurring at  $\eta_5$ , bands v2 and v1 touch each other at the  $\mathbf{K}$  point in the BZ [Fig. 8(e)], and hence for both bands a topological phase transition takes place at this point.

Further, along  $L_3$ , again multiple phase transitions occur [see Figs. 7(b) and 7(d)], and the corresponding dispersions are shown in Figs. 8(g)–8(o). At  $\gamma_1$ , bands v2 and v1 show

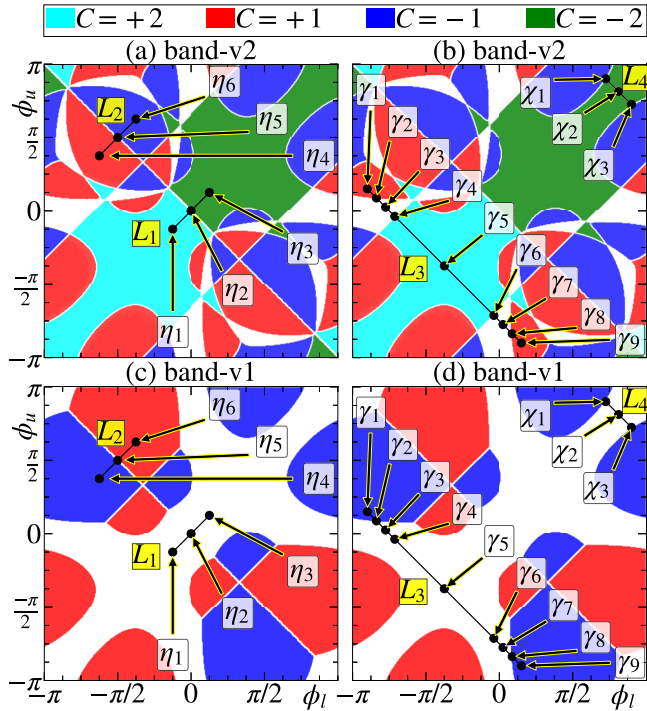


FIG. 7. The phase diagrams corresponding to band v2 are shown in (a) and (b), and those for band v1 are presented in (c) and (d). In (a) and (c), the  $\eta$  points are used and shown along the  $L_1$  and  $L_2$  lines, whereas the  $\gamma$  and  $\chi$  points are marked along the  $L_3$  and  $L_4$  lines in both (b) and (d). Along those lines multiple phase transitions occur. For example, along  $L_3$ , the Chern number corresponding to band v2 has values  $+1, 0, +2, 0,$  and  $+1$  at the points  $\gamma_1, \gamma_3, \gamma_5, \gamma_7,$  and  $\gamma_9$ , respectively. The phase transitions take place at  $\gamma_2, \gamma_4, \gamma_6,$  and  $\gamma_8$ , where band v2 touches either band v1 or band c2. The values of  $t_\perp$  and  $t_1$  are taken as  $0.5t$  and  $t$ , respectively.

$C = +1$  and  $C = -1$ , respectively, which drops to zero at  $\gamma_2$ , and hence the gap between those bands closes at the  $\mathbf{K}$  point, as shown in Fig. 8(h). At  $\gamma_3$  the gap reopens, but the Chern numbers corresponding to these bands remain zero. The gap between bands v2 and c2 vanishes at  $\gamma_4$ , where again a phase transition takes place, since along the line connecting  $\gamma_4$  and  $\gamma_6$ , the Chern number has a value  $+2$ . The band structure at an intermediate point, namely,  $\gamma_5$ , is shown in Fig. 8(k). Similarly, phase transitions take place at  $\gamma_6$  and  $\gamma_8$ , where the gaps vanish at the  $\mathbf{K}'$  point. At  $\gamma_7$  and  $\gamma_9$ ,  $C$  assumes values of zero and  $+1$ , respectively, corresponding to band v2. It should be noted that band v1 shows vanishing of the Chern number between  $\gamma_2$  and  $\gamma_8$  segments [see Fig. 7(d)] and hence it never touches band v2, which results in the absence of any phase transition.

We now show the phase transitions between the  $C = -2$  and  $C = -1$  phase along  $L_4$ . The corresponding band structures are shown in Figs. 8(p)–8(r). At  $\chi_2$ , band v2 and band v1 remain isolated from each other; however, they possess Chern numbers  $C = -2$  and  $C = 0$ , respectively. At  $\chi_1$  and  $\chi_3$ , these two bands touch each other at the  $\mathbf{K}'$  and  $\mathbf{K}$  points in the BZ, respectively, where topological phase transitions take place. Beyond  $\chi_1$  and  $\chi_3$ , the gap reopens and both bands possess nontrivial phases with  $C = -1$ .

Further, along the  $\phi_u = -\phi_l$  line, a semimetallic phase exists for all the bands. In the vicinity of  $\phi_u = \phi_l$ , only the phase diagrams of band v1 show trivial regions with  $C = 0$ ; however, those for band v2 demonstrate nontrivial phases either with  $C = +2$  or  $C = -2$ .

Moreover, in order to see the effects of  $t_\perp$  on the topological phases, we have shown the phase diagrams corresponding to bands v1 and v2 in Figs. 9(a)–9(d) and 9(e)–9(h), respectively. It is evident that the areas of Chern insulating regions are enhanced corresponding to lower values of  $t_\perp$ . Also, the shapes of the topological regions are different from those for the  $t_\perp = 0.5t$  case. Further, the areas of  $C = \pm 2$  regions in the phase diagram corresponding to band v2 are mostly spanned by the  $C = \pm 1$  regions. However, the feature that remains unaltered is the trivial phase along  $\phi_u = \pm\phi_l$  lines for band v1 and the  $\phi_u = \phi_l$  line for band v2. For both  $t_\perp = 0.5t$  and  $t_\perp = 0.1t$ , the Chern insulating regions gradually shrink with the increase in the value of  $t_1$  and finally vanish at the semi-Dirac limit, namely,  $t_1 = 2t$ .

## V. EDGE STATES

To show the existence (and their vanishing) of the edge modes, in this section we show the band structure of the system for semi-infinite nanoribbon. The ribbon has a finite width along the  $y$  direction, while it is infinite along the  $x$  direction [40,41]. Further, we label the sites along the  $y$  direction as  $A_1^l, B_1^l, A_2^l, B_2^l, \dots, A_N^l, B_N^l, A_1^u, B_1^u, A_2^u, B_2^u, \dots, A_N^u, B_N^u$ . Since the periodicity along the  $x$  direction remains preserved, we can Fourier transform the operators along that direction. This results in set of four coupled equations as shown below:

$$E_k a_{k,n}^u = [t\{1 + e^{(-1)^n ik}\}b_{k,n}^u + t_1 b_{k,n-1}^u - 2t_2 \left[ \cos(k + \phi)a_{k,n}^u + e^{(-1)^n \frac{k}{2}} \times \cos\left(\frac{k}{2} - \phi\right)\{a_{k,n-1}^u + a_{k,n+1}^u\} \right], \quad (11)$$

$$E_k b_{k,n}^u = [t\{1 + e^{(-1)^{n+1} ik}\}a_{k,n}^u + t_1 a_{k,n+1}^u - 2t_2 \left[ e^{(-1)^{n+1} \frac{k}{2}} \times \cos\left(\frac{k}{2} + \phi\right)\{a_{k,n-1}^u + a_{k,n+1}^u\} + \cos(k - \phi)b_{k,n}^u \right] + t_\perp [\xi_1 e^{-ik} + \xi_2] a_n^l, \quad (12)$$

$$E_k a_{k,n}^l = [t\{1 + e^{(-1)^n ik}\}b_{k,n}^l + t_1 b_{k,n-1}^l - 2t_2 \left[ e^{(-1)^n \frac{k}{2}} \times \cos\left(\frac{k}{2} - \phi\right)\{a_{k,n-1}^l + a_{k,n+1}^l\} \times \cos(k + \phi)a_{k,n}^l \right] + t_\perp [\xi_1 e^{ik} + \xi_2] b_n^u \quad (13)$$

$$E_k b_{k,n}^l = [t\{1 + e^{(-1)^{n+1} ik}\}a_{k,n}^l + t_1 a_{k,n+1}^l - 2t_2 \left[ \cos(k - \phi)b_{k,n}^l + e^{(-1)^{n+1} \frac{k}{2}} \times \cos\left(\frac{k}{2} + \phi\right)\{a_{k,n-1}^l + a_{k,n+1}^l\} \right], \quad (14)$$

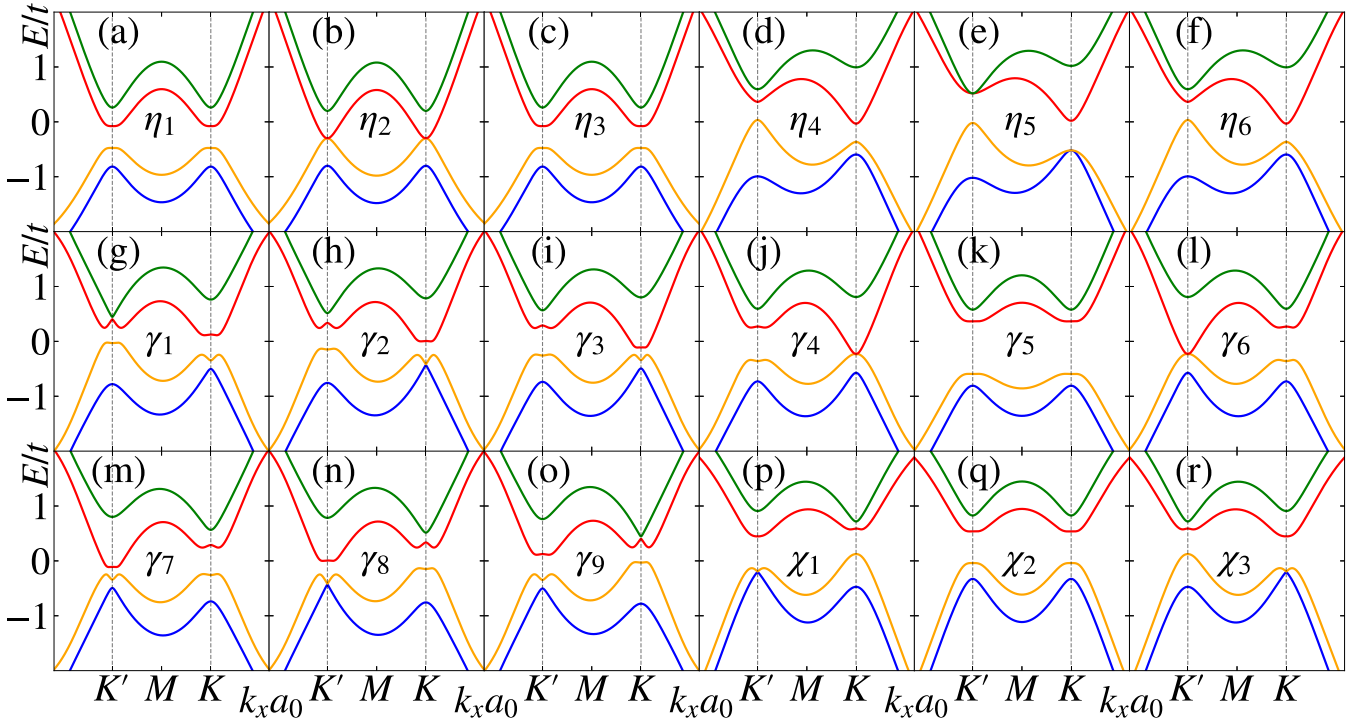


FIG. 8. The band structures corresponding to the points  $\eta_1 - \eta_6$  [shown in Figs. 7(a) and 7(c)] are depicted in [(a)–(f)]. The spectra for the points  $\gamma_1 - \gamma_9$  [shown in Figs. 7(b) and 7(d)] are shown in [(g)–(o)], and for the points  $\chi_1 - \chi_3$  are presented in [(p)–(r)]. The values of  $t_1$  and  $t_\perp$  for all the band structures are kept fixed at  $t$  and  $0.5t$ , respectively.

where  $a_{k,n}^{l,u}$  and  $b_{k,n}^{l,u}$  are the amplitudes of the wave functions corresponding to the sublattices A and B, respectively. The superscripts  $l$  and  $u$  refer to lower and upper layers, respectively. Here  $k = \sqrt{3}k_x a_0$  is the dimensionless momentum and  $n$  denotes the site index, which assumes integer values in the range  $[1 : N]$ , with  $N$  being the total number of unit cells along the  $y$  direction. We chose  $N$  as 128, which gives the width to

be  $79\sqrt{3}a_0$ . In Eqs. (12) and (13),  $\xi_1$  and  $\xi_2$  denote quantities that depend on the site index  $n$  via  $\xi_1 = [1 - (-1)^n]/2$  and  $\xi_2 = [1 + (-1)^n]/2$ , respectively.

By solving Eqs. (11)–(14), we obtain the band structure of the nanoribbon for various values of  $t_1$  as presented in Fig. 10. It can be noticed that a pair of edge modes from the valence bands (band v2) traverse the Fermi level  $E_F$  (shown via the red dashed line) and merge with the conduction bands (band c2), and another pair crosses the Fermi level in the opposite direction. Such crossing of the edge modes leads to a quantized Hall conductivity should the Fermi level lie in the bulk gap.  $E_F$  intersects the edge modes [see Figs. 10(a) and 10(b)] at four points (marked by the green dots) whose corresponding edge currents are shown by the green arrows in the yellow panels located at the top right corner of the plots. The yellow panels represent a part of the semi-infinite ribbon. Since the velocity of electrons is proportional to the slope of the band structure, that is,  $\partial E/\partial k$ , there exists a pair of edge currents at each edge that moves in the same direction. However, such pairs of currents propagate in opposite directions at the two edges of the ribbon. Hence, these modes are called chiral edge modes.

It should be noted that because of a pair of chiral edge modes, we should obtain the Hall conductivity quantized with a plateau at  $2e^2/h$ , with the factor “2” arising due to doubling of the number of chiral edge modes [42]. Such chiral edge modes exist as long as the value of  $t_1$  remains less than  $2t$ . Since the bulk gap vanishes at  $t_1 = 2t$  [see Fig. 10(c)], the edge current vanishes. For  $t_1 > 2t$ , the edge modes get detached from the bulk bands as shown in Fig. 10(d) for  $t_1 = 2.2t$ , thereby resulting in a zero edge current. These

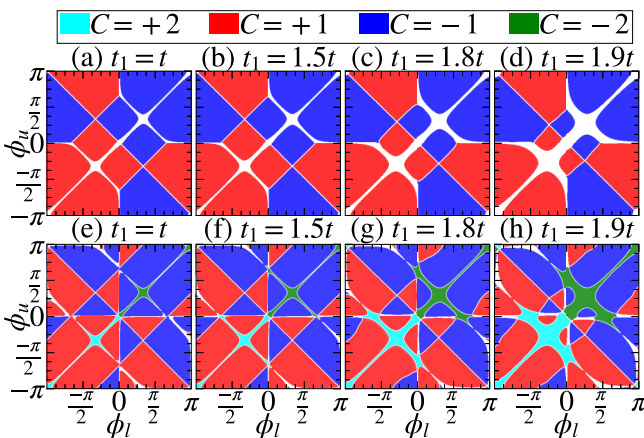


FIG. 9. The phase diagrams corresponding to band v1 are shown in [(a)–(d)], while those for band v2 are shown in [(e)–(h)]. The value of  $t_\perp$  is kept fixed at  $0.1t$ . The values of  $t_1$  are such that  $t_1 = t$  in (a) and (e),  $t_1 = 1.5t$  in (b) and (f),  $t_1 = 1.8t$  in (c) and (g), and  $t_1 = 1.9t$  in (d) and (h). The white regions denote trivial phases with zero Chern numbers, while the colored regions indicate the nontrivial phases with the nonzero Chern numbers. The values are indicated at the top of the figure.



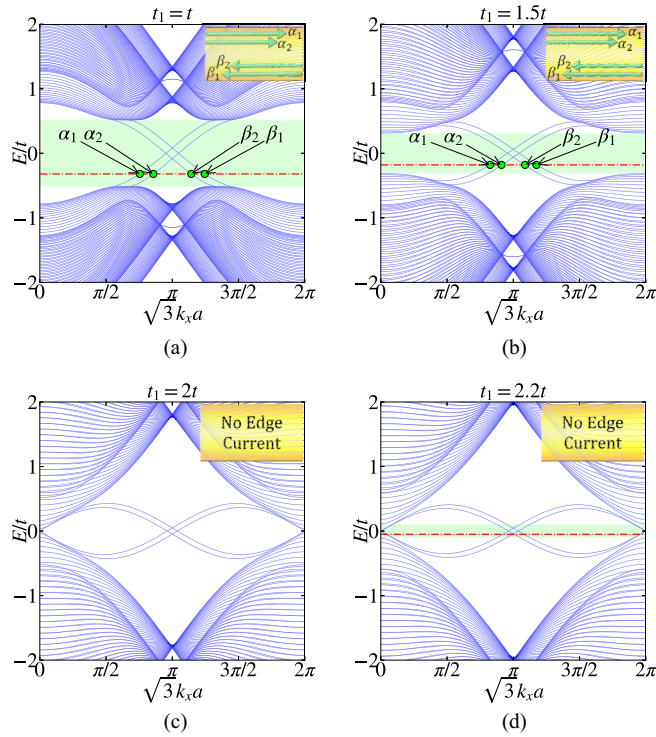


FIG. 10. The edge state spectra are shown for (a)  $t_1 = t$ , (b)  $t_1 = 1.5t$ , (c)  $t_1 = 2t$ , and (d)  $t_1 = 2.2t$ . The green shaded regions represent the bulk gap in (a), (b), and (d) [no bulk gap in (c)]. The Fermi levels ( $E_F$ ) are denoted by the red dashed lines, which are shown to be present in the bulk gap.  $E_F$  intersects the edge modes at the points denoted by the green dots as shown in (a) and (b). For these, the edge currents are shown by the green arrows in the yellow panels located at the top right corner, which represent parts of the semi-infinite ribbon.

results are consistent with the corresponding Chern numbers obtained in the phase diagram. For example, we observe the nonzero edge currents for  $t_1 < 2t$ , and the corresponding Chern number is found to be  $C = |2|$ . For  $t_1 > 2t$ , the Chern numbers vanish, and so do the edge currents. The figures presented here are for  $t_\perp = 0.5t$ . For  $t_\perp = 0.1t$ , we observe similar features in the spectrum, except that the bulk gaps are reduced. We have skipped the discussion of the latter for brevity.

## VI. HALL CONDUCTIVITY

In this section we calculate the anomalous Hall conductivity as function of the Fermi energy  $E_F$ . The prerequisite is the computation of the Berry curvature using Eq. (10), and hence use the following formula to calculate the anomalous Hall conductivity ( $\sigma_{xy}$ ) [43,44], namely,

$$\sigma_{xy} = \frac{\sigma_0}{2\pi} \sum_{\lambda} \int \frac{dk_x dk_y}{(2\pi)^2} f(E_{k_x, k_y}^{\lambda}) \Omega(k_x, k_y), \quad (15)$$

where  $f(E_{k_x, k_y}^{\lambda}) = [1 + \exp\{(E_{k_x, k_y}^{\lambda} - E_F)/K_B T\}]^{-1}$  is the Fermi-Dirac distribution function at an energy  $E_{k_x, k_y}^{\lambda}$ . Here  $E_F$  refers to the Fermi energy and  $T$  is the absolute temperature. The energy is denoted by  $E_{k_x, k_y}^{\lambda}$  with  $\lambda$  being the band index. The constant term  $\sigma_0$  is equal to  $e^2/h$ , which sets the scale for  $\sigma_{xy}$ . Now, we compute  $\sigma_{xy}$  numerically as a function of  $E_F$  at

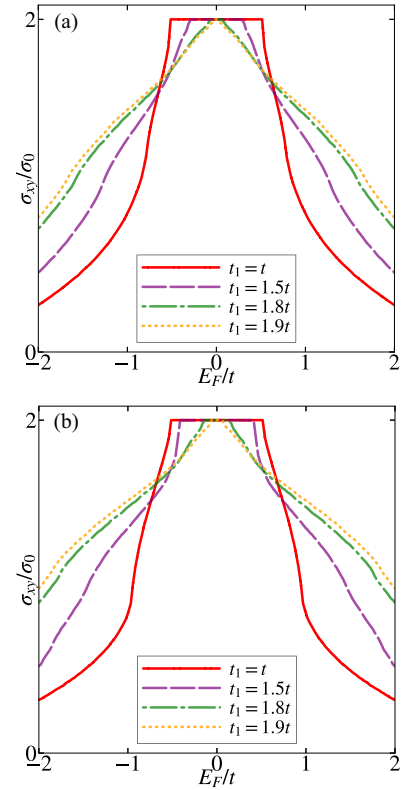


FIG. 11. The anomalous Hall conductivities are shown as a function of  $E_F$  for various values of  $t_1$  in (a) and (b) for  $t_\perp = 0.5t$  and  $t_\perp = 0.1t$ , respectively. The plateau width decreases as  $t_1$  deviates from  $t$ .

zero temperature ( $T = 0$ ) for various values of  $t_1$  as shown in Fig. 11.

As can be seen from Fig. 11(a) that when the Fermi energy  $E_F$  lies in the bulk gap,  $\sigma_{xy}$  becomes quantized at a value  $2\sigma_0$ . The width of the plateau is equal to the width of the bulk gap in the dispersion spectrum of Fig. 2. As soon as  $E_F$  intersects the bands (either both the conduction or both the valence bands),  $\sigma_{xy}$  starts to decrease since the integral is performed over the occupied states. This also results in diminishing of the plateau width with increase in the value of  $t_1$ . This happens because the energy gap between the band c2 and band v2 shrinks. The plateau and the Hall conductivity vanish completely at  $t_1 = 2t$ , where the spectrum becomes gapless. For the hopping asymmetry engineered beyond the semi-Dirac limit, that is,  $t_1 > 2t$ , the bands become gapped again; however, the Hall conductivity remains zero. These results are consistent with their corresponding information coming from the Chern numbers. The Hall plateaus are observed as long as the system remains a Chern insulator, that is, for  $t_1 < 2t$ . Further, the factor 2 in ( $2\sigma_0$ ) denotes the value of Chern number (and also the edge modes), which vanishes for  $t_1 > 2t$ .

We have also presented the Hall conductivity for a smaller value of  $t_\perp$ , namely,  $t_\perp = 0.1t$  in Fig. 11(b). In this case the plateau widths corresponding to different values of  $t_1$  are larger as compared to that for the  $t_\perp = 0.5t$  case, since the corresponding band gaps are enhanced as shown in Fig. 3. However, similar to the previous case, the plateau width decreases with the increase of  $t_1$ , which finally vanishes at



$t_1 = 2t$  and beyond. Thus a topological phase transition takes place across the gap closing point at the semi-Dirac limit, namely,  $t_1 = 2t$ .

## VII. CONCLUSION

We have investigated the topological properties for a band-engineered bilayer Haldane. By tuning one of the three NN hopping amplitudes, the band extrema, which were located at the  $\mathbf{K}$  and  $\mathbf{K}'$  points for the Dirac case, migrate towards each other and finally merge at an intermediate  $\mathbf{M}$  point in the BZ in the semi-Dirac limit, that is, at  $t_1 = 2t$ . We have calculated the Chern numbers for various values of  $t_1$  and plotted them in the  $\phi_u - \phi_l$  plane, which demonstrates that the higher Chern numbers ( $C = \pm 2$ ) are associated only with band v2. However, the Chern numbers corresponding to both bands vanish, that is, there are topological phase transitions where the Chern numbers discontinuously change from

$C = \pm 2$  to  $C = 0$  and  $C = \pm 1$  to  $C = 0$ , across the semi-Dirac point  $t_1 = 2t$ . Also, there are multiple phase transitions in the phase diagram, such as,  $+2 \rightarrow -2$ ,  $+1 \rightarrow -1$ ,  $\pm 2 \rightarrow \pm 1$ , and  $\pm 2 \rightarrow 0 \rightarrow 1$ . These phase transitions are confirmed by the opening and closing of the energy gaps (semimetallic phase) in the dispersion spectrum. Further, we have also computed the band structure of a nanoribbon, where we observe a pair of chiral edge modes along the edges of the ribbon exist as long as  $t_1$  remains less than  $2t$ . Also, for the anomalous Hall conductivity, the width of the quantized plateau at  $2\sigma_0$  gradually decreases with increase in  $t_1$ , which finally vanishes at  $t_1 = 2t$ . Thus, a bilayer Haldane model, similar to its monolayer analog, exhibits a topological phase transition at the semi-Dirac point. However, here we have larger Chern number values and doubling of the edge modes at the edges of the bilayer nanoribbon. Further, the phase transitions are supported by the vanishing Chern number, chiral edge modes, and the anomalous Hall conductivity.

- 
- [1] F. D. M. Haldane, *Phys. Rev. Lett.* **61**, 2015 (1988).  
 [2] S. Spurrier and N. R. Cooper, *Phys. Rev. Res.* **2**, 033071 (2020).  
 [3] P. Cheng, P. W. Klein, K. Plekhanov, K. Sengstock, M. Aidelburger, C. Weitenberg, and K. Le Hur, *Phys. Rev. B* **100**, 081107(R) (2019).  
 [4] S. Sorn, *Phys. Rev. B* **98**, 125145 (2018).  
 [5] J. Panas, B. Irisigler, J.-H. Zheng, and W. Hofstetter, *Phys. Rev. B* **102**, 075403 (2020).  
 [6] Y. Xiao, J. Liu, and L. Fu, *Matter* **3**, 1142 (2020).  
 [7] Y.-Z. You and A. Vishwanath, *npj Quantum Mater.* **4**, 16 (2019).  
 [8] Q. Tong, H. Yu, Q. Zhu, Y. Wang, X. Xu, and W. Yao, *Nat. Phys.* **13**, 356 (2017).  
 [9] C. N. Lau, M. W. Bockrath, K. F. Mak, and F. Zhang, *Nature (London)* **602**, 41 (2022).  
 [10] E. Y. Andrei, D. K. Efetov, P. J. Herrero, A. H. MacDonald, K. F. Mak, T. Senthil, E. Tutuc, A. Yazdani, and A. F. Young, *Nat. Rev. Mater.* **6**, 201 (2021).  
 [11] S. Mondal, P. Kapri, B. Dey, T. K. Ghosh, and S. Basu, *J. Phys.: Condens. Matter* **33**, 225504 (2021).  
 [12] S. Mondal and S. Basu, *Phys. Rev. B* **105**, 235441 (2022).  
 [13] S. Mondal and S. Basu, *Phys. Rev. B* **107**, 035421 (2023).  
 [14] V. Pardo and W. E. Pickett, *Phys. Rev. Lett.* **102**, 166803 (2009).  
 [15] V. Pardo and W. E. Pickett, *Phys. Rev. B* **81**, 035111 (2010).  
 [16] A. S. Rodin, A. Carvalho, and A. H. Castro Neto, *Phys. Rev. Lett.* **112**, 176801 (2014).  
 [17] J. Guan, Z. Zhu, and D. Tománek, *Phys. Rev. Lett.* **113**, 046804 (2014).  
 [18] Y. Suzumura, T. Morinari, and F. Piéchon, *J. Phys. Soc. Jpn.* **82**, 023708 (2013).  
 [19] Y. Hasegawa, R. Konno, H. Nakano, and M. Kohmoto, *Phys. Rev. B* **74**, 033413 (2006).  
 [20] J. Kim, S. S. Baik, S. H. Ryu, Y. Sohn, S. Park, B.-G. Park, J. Denlinger, Y. Yi, H. J. Choi, and K. S. Kim, *Science* **349**, 723 (2015).  
 [21] C. Zhong, Y. Chen, Y. Xie, Y.-Y. Sun, and S. Zhang, *Phys. Chem. Chem. Phys.* **19**, 3820 (2017).  
 [22] D. Sticlet and F. Piéchon, *Phys. Rev. B* **87**, 115402 (2013).  
 [23] S. Mondal and S. Basu, *Phys. Rev. B* **105**, 235409 (2022).  
 [24] S. Yang, Z.-C. Gu, K. Sun, and S. Das Sarma, *Phys. Rev. B* **86**, 241112(R) (2012).  
 [25] W.-C. Chen, R. Liu, Y.-F. Wang, and C.-D. Gong, *Phys. Rev. B* **86**, 085311 (2012).  
 [26] Y. Yang, Y. F. Zhang, L. Sheng, and D. Y. Xing, *Europhys. Lett.* **105**, 27005 (2014).  
 [27] Y. Yang, X. Li, and D. Xing, *Eur. Phys. J. B* **89**, 217 (2016).  
 [28] A. Alase and D. L. Feder, *Phys. Rev. A* **103**, 053305 (2021).  
 [29] M. Łącki, J. Zarkzewski, and N. Goldman, *SciPost Phys.* **10**, 112 (2021).  
 [30] C. Fang, M. J. Gilbert, and B. A. Bernevig, *Phys. Rev. Lett.* **112**, 046801 (2014).  
 [31] J. Wang, B. Lian, H. Zhang, Y. Xu, and S.-C. Zhang, *Phys. Rev. Lett.* **111**, 136801 (2013).  
 [32] W. Zhu, C. Song, H. Bai, L. Liao, and F. Pan, *Phys. Rev. B* **105**, 155122 (2022).  
 [33] J. Ge, Y. Liu, J. Li, H. Li, T. Luo, Y. Wu, Y. Xu, and J. Wang, *Natl. Sci. Rev.* **7**, 1280 (2020).  
 [34] Y. F. Zhao, R. Zhang, R. Mei, L. Zhou, H. Yi, Y. Q. Zhang, J. Yu, R. Xiao, K. Wang, N. Samarth, M. H. W. Chan, C. X. Liu, and C. Z. Chang, *Nature (London)* **588**, 419 (2020).  
 [35] H. Zhao, T. Zhang, X. Zhang, M.-H. Lu, and Y.-F. Chen, *Front. Phys.* **10**, 844417 (2022).  
 [36] However, for obtaining the Chern number phase diagrams, see Figs. 4, 5, and 9,  $\phi_l$  and  $\phi_u$  are varied in the range  $[-\pi : +\pi]$ .  
 [37] D. J. Thouless, *Topological Quantum Numbers in Nonrelativistic Physics* (World Scientific, Singapore, 1998).  
 [38] J. E. Avron, L. Sadun, J. Segert, and B. Simon, *Phys. Rev. Lett.* **61**, 1329 (1988).  
 [39] C.-X. Liu, S.-C. Zhang, and X.-L. Qi, *Annu. Rev. Condens. Matter Phys.* **7**, 301 (2016).  
 [40] D. Sticlet, F. Piéchon, J.-N. Fuchs, P. Kalugin, and P. Simon, *Phys. Rev. B* **85**, 165456 (2012).  
 [41] K. Nakada, M. Fujita, G. Dresselhaus, and M. S. Dresselhaus, *Phys. Rev. B* **54**, 17954 (1996).  
 [42] Y. Hatsugai, *Phys. Rev. B* **48**, 11851 (1993).  
 [43] D. Xiao, M.-C. Chang, and Q. Niu, *Rev. Mod. Phys.* **82**, 1959 (2010).  
 [44] D. Culcer, A. MacDonald, and Q. Niu, *Phys. Rev. B* **68**, 045327 (2003).